Published OnlineFirst October 29, 2012; DOI:10.1158/0008-5472.CAN-12-2670

Spatiotemporal Assessments of Dermal Hyperemia Enable Accurate Prediction of Experimental Cutaneous Carcinogenesis as well as Chemopreventive Activity

Raymond L. Konger[1,2], Zhengbin Xu[3], Ravi P. Sahu[1,2], Badri M. Rashid[1], Shama R. Mehta[1], Deena R. Mohamed[1], Sonia C. DaSilva-Arnold[1,2], Joshua R. Bradish[1], Simon J. Warren[1,2], and Young L. Kim[3]

Abstract

Field cancerization refers to areas of grossly normal epithelium that exhibit increased risk for tumor occurrence. Unfortunately, elucidation of the locoregional changes that contribute to increased tumor risk is difficult due to the inability to visualize the field. In this study, we use a noninvasive optical-based imaging approach to detail spatiotemporal changes in subclinical hyperemia that occur during experimental cutaneous carcinogenesis. After acute inflammation from 10 weeks of UVB irradiation subsides, small areas of focal hyperemia form and were seen to persist and expand long after cessation of UVB irradiation. We show that these persistent early hyperemic foci reliably predict sites of angiogenesis and overlying tumor formation. More than 96% of the tumors (57 of 59) that developed following UVB or 7,12-dimethylbenz(a)anthracene/phorbol 12-myristate 13-acetate (DMBA/PMA) treatment developed in sites of preexisting hyperemic foci. Hyperemic foci were multifocal and heterogeneously distributed and represented a minor fraction of the carcinogen-treated skin surface (10.3% of the imaging area in vehicle-treated animals). Finally, we also assessed the ability of the anti-inflammatory agent, celecoxib, to suppress hyperemia formation during photocarcinogenesis. The chemopreventive activity of celecoxib was shown to correlate with its ability to reduce the area of skin that exhibit these hyperemic foci, reducing the area of imaged skin containing hyperemic foci by 49.1%. Thus, we propose that a hyperemic switch can be exploited to visualize the cancerization field very early in the course of cutaneous carcinogenesis and provides insight into the chemopreventive activity of the anti-inflammatory agent celecoxib. *Cancer Res; 73(1); 150–9. ©2012 AACR.*

Introduction

Field cancerization describes the increased risk for additional tumor formation following the appearance of a first tumor within an area exposed to carcinogens (e.g., UVB; refs. 1–3). However, the exact nature of the field involvement is unclear as the "field" generally cannot be visualized but is established *post hoc* after tumor(s) begin to appear. Recently, fiber-optic endoscope-based measurements of superficial hemoglobin (Hb) content at multiple random sites have shown that a measurable early increase in blood supply (EIBS) is detected not only in the tumor stromal environment, but is also seen in the histologically normal mucosa of the gastrointestinal tract in areas both near and remote from the neoplastic lesion (4, 5). Moreover, EIBS may occur very early during tumorigenesis, as EIBS is seen before tumor formation in the normal colonic mucosa of azoxymethane-treated rats compared with the colons of vehicle-treated rats (6). The authors also showed that the increased hyperemia represents increased angiogenesis (6). Thus, this group proposes that EIBS is a feature of field cancerization (6). Unfortunately, these studies use random point measurements taken with a probe-based optical sensor and are limited in that they fail to visualize EIBS across a carcinogenic field. Thus, it is unclear whether EIBS exhibits a direct correlation with sites in which tumors will eventually form or represent a homogenous change to the entire field at risk.

Studies using painstaking microscopic examination of tissues have also indicated that angiogenesis can occur relatively early in tumor development (7). In this case, angiogenesis was associated with early hyperplastic changes that were multifocally or nonhomogenously distributed (7). Regrettably, the process of obtaining tissue samples for microscopic examination results in the inability to monitor these sites of angiogenesis and hyperplasia over time to verify their association with future malignancy. Thus, while these data suggest that hyperemia within the (pre)carcinogenic field is heterogeneously or multifocally distributed, the question remains as to whether these sites are spatially fixed over time. Given the inability to

Authors' Affiliations: Departments of [1]Pathology and Laboratory Medicine and [2]Dermatology, Indiana University School of Medicine, Indianapolis; and [3]Weldon School of Biomedical Engineering, Purdue University, West Lafayette, Indiana

Note: Supplementary data for this article are available at Cancer Research Online (http://cancerres.aacrjournals.org/).

Corresponding Author: Young L. Kim, Weldon School of Biomedical Engineering, Purdue University, West Lafayette, IN 47907. Phone: 765-496-2445; Fax: 765-496-1459; E-mail: youngkim@purdue.edu

doi: 10.1158/0008-5472.CAN-12-2670

©2012 American Association for Cancer Research.

Downloaded from cancerres.aacrjournals.org on January 3, 2013
Copyright © 2013 American Association for Cancer Research

Published OnlineFirst October 29, 2012; DOI:10.1158/0008-5472.CAN-12-2670

determine *a priori* the specific site in which a tumor is likely to occur, microenvironmental changes necessary for tumor development could be missed or their significance underestimated if they are nonhomogenous in distribution, represent a minor fraction of the available surface, or are not visible on clinical inspection. In contrast, changes seen over the whole field may be readily apparent, but their importance to tumorigenesis may be overestimated. Thus, while we have experienced tremendous growth in our understanding of the microenvironment that surrounds visible tumors, we have a more limited understanding of the premalignant microenvironment due to the inability to target studies to specific sites of future tumor appearance within a cancerization field (8).

The idea that angiogenesis is turned on early during carcinogenesis is supported by studies in human tumors and in mouse models of multistage chemical carcinogenesis (7, 9–11). While the mechanisms for this early induction of angiogenesis during tumorigenesis are incompletely understood, existing tumors are known to induce angiogenesis by increased production of proangiogenic inflammatory cytokines/chemokines (inflammatory angiogenesis; refs. 10, 12). Moreover, the majority of human cancers are thought to be derived from environmental exposures and lifestyle choices (13–15). Importantly, a common feature of these environmental and lifestyle choices is that they promote inflammatory angiogenesis (10, 14, 16, 17). The importance of inflammatory angiogenesis in early stages of tumorigenesis may also be inferred by the ability of a number of chemopreventive agents, such as the anti-inflammatory COX-2 inhibitors, to suppress both the inflammation and angiogenesis that are observed following the application of carcinogenic insults (10, 14, 16, 17).

In this study, we use a novel technique that couples optical measurement of Hb content to a noninvasive imaging platform in live animals to determine detailed spatiotemporal patterns of hyperemia formation in a large area (15 mm × 45 mm) during the course of cutaneous chemical and photocarcinogenesis. We then correlate the areas of hyperemia with subsequent tumor formation to verify that this methodology visualizes the (pre)carcinogenic field. Given the known ability of celecoxib to act as an anti-inflammatory and antiangiogenic chemopreventive agent, we also examine the effects of celecoxib on the spatiotemporal extent of hyperemia formation. We propose that this new approach to visualize EIBS provides a novel method to noninvasively visualize field cancerization early in the course of cutaneous carcinogenesis.

Materials and Methods

Chemical carcinogenesis study

Eight female FVB/n mice were treated with 7,12-dimethylbenz(a)anthracene/phorbol 12-myristate 13-acetate (DMBA/PMA) as previously described (18). After shaving and depilatory cream application to remove hair from the imaging area, the mice were imaged and Hb content assessed as described (18).

Photocarcinogenesis studies

SKH-1 hairless albino mice (Charles River Laboratories) were irradiated with 1 minimal erythema dose of UVB (2,240 J/m^2) 3 times per week (Monday, Wednesday, and Friday) as previously described (19). Studies by us and others have shown that this treatment consistently results in initial tumor formation within 11 to 12 weeks of treatment (19, 20). We therefore discontinued UVB treatments after 10 weeks of treatment. This resulted in a cumulative UVB dose of 67.2 kJ/m^2, which exceeds a known carcinogenic cumulative UVB dose of 26.2 kJ/m^2 (21). For celecoxib studies (20), a chemopreventive dose of 0.5 mg of celecoxib (LC Laboratories) in 0.2 mL acetone (or vehicle alone) was applied topically immediately after each UVB irradiation and 3 times per week after discontinuation of the UVB irradiations. We imaged the irradiated mouse skin every 2 weeks, using our microvascular imaging platform (22, 23; Supplementary Methods and Supplementary Figs. S1–S3 for detailed performance characteristics). To obtain sequential images from identical areas over time, we had reference tattoos placed on each mouse to form a rectangular imaging grid. The mice were lightly sedated using ketamine/xylazine for immobilization during imaging.

Histopathologic assessment for neoplastic lesions

Visible tumors were scored on a weekly basis when exophytic growths exceeding 1 mm in diameter were observed. At the end of the study (20 weeks after discontinuing UVB treatments), all visible tumors were removed and formalin-fixed for tumor classification by a dermatopathologist. In addition, skin from areas of high and low Hb content that did not contain visibly apparent tumors were removed and were formalin-fixed. Paraffin-embedded sections were stained with hematoxylin and eosin (H&E) and examined by dermatopathologists for the presence of small tumors not visible macroscopically. Tumors were classified as previously described ref. 19 and Supplementary Methods).

Microvascular density

Following heat-induced antigen retrieval in citrate buffer, pH 6.0, formalin-fixed paraffin-embedded tissue slides were subjected to immunolabeling using rat monoclonal anti-mouse CD31 antibodies (Clone SZ31, Dianova). Stained sections were blinded and 5 random 400× fields per tissue section were counted by 3 different individuals. Microvessels were only counted where a visible lumen was observed. The mean value derived from the microvascular density (MVD) counts from all 3 individuals was used for data presentation and statistical analysis.

Statistical analysis

Nonparametric and parametric statistical analysis was used where appropriate (Supplementary Methods). Statistical significance was assigned at a P value less than 0.05.

Results

Imaging of microvascular Hb content during chemical carcinogenesis and photocarcinogenesis shows that EIBS precedes visible tumor occurrence

We first used a DMBA/PMA chemical carcinogenesis protocol to examine the spatiotemporal changes in Hb

Downloaded from cancerres.aacrjournals.org on January 3, 2013
Copyright © 2013 American Association for Cancer Research

Published OnlineFirst October 29, 2012; DOI:10.1158/0008-5472.CAN-12-2670

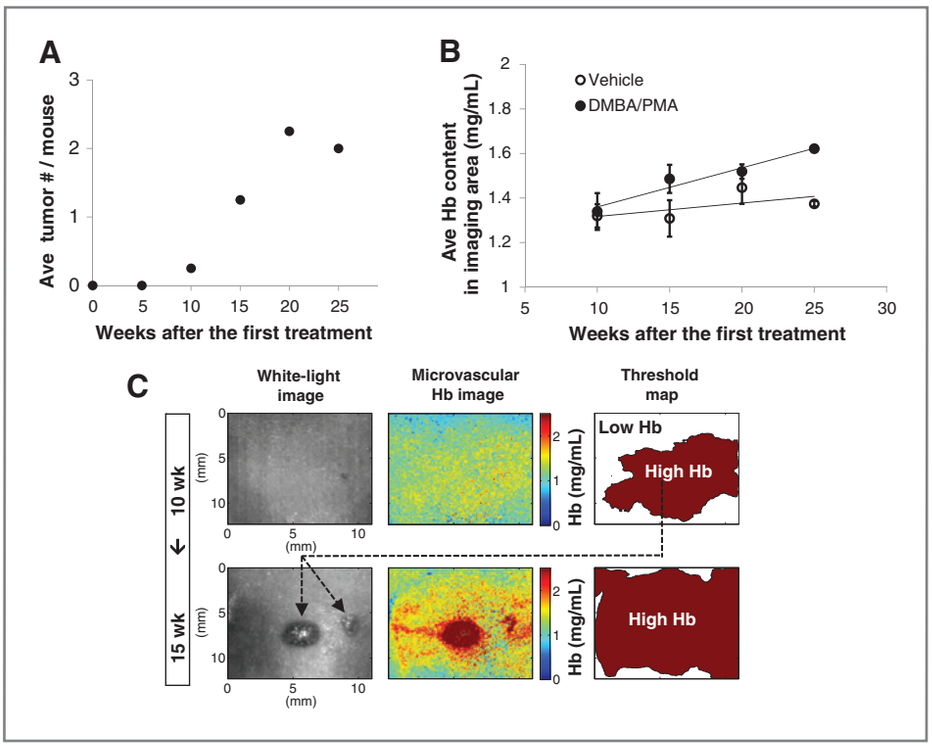


Figure 1. During chemical carcinogenesis, tumors develop in regions of focal hyperemia. FVB/n mice were treated with a single dose of DMBA and repeated dosing with PMA and then followed for tumor occurrence and sequential imaging. A, visible tumor multiplicity in mice treated with DMBA/PMA. B, averaged Hb content within the imaging area (acetone)-treated mice shows a significant increase in Hb content over time for DMBA/PMA–treated mice, but not for vehicle-treated mice. For the DMBA/PMA group, the slope estimate of the linear regression for Hb content over time was significantly greater than 0 ($P = 0.027$). The slope of the regression line for the vehicle group was not significantly different from 0 ($P = 0.383$). Moreover, there was a significant difference in the slope estimates between DMBA/PMA–treated and vehicle-treated mice ($P = 0.007$). C, hyperemia precedes grossly visible tumor formation. Top (10 weeks after the first carcinogen treatment): left, white-light image (no visible lesion); middle, Hb content; and right, threshold mapping to define areas of high Hb content. Bottom (5 weeks later): tumors now visible along with expansion of the hyperemic area. Of 9 tumors observed in the imaging area, all occurred in areas of persistent hyperemia.

content during cutaneous carcinogenesis (18). As expected, DMBA/PMA–treated mice developed tumors within 10 weeks of initiating treatment, eventually reaching approximately 2 tumors per mouse (Fig. 1A). Nine durable tumors occurred within the 12 mm × 12 mm imaging area. Overall averaged Hb content within the imaging area was unchanged in the DMBA/PMA–treated mice relative to vehicle control mice before 10 weeks but was increased in the DMBA/PMA–treated mice beginning at week 10 (Fig. 1B). Although the increased Hb content correlates with increasing tumor burden (Fig. 1C, right), we noted that all 9 tumors were seen to develop in focal areas of hyperemia that were apparent before the visible appearance of tumors. This indicates that hyperemia may represent an early step in tumorigenesis. We next mapped out progressively smaller areas of increased Hb content by using sequentially higher Hb cutoffs for threshold mapping (Fig. 1C). We found that all tumors occurred in preexisting areas of Hb content more than 1.6 mg/mL (20.4% of the imaged area). These observations suggest that our imaging methodology was measuring EIBS during early tumorigenesis. Unfortunately, the DMBA/PMA model had several deficiencies. First, the need for shaving and the use of depilatory creams made imaging difficult and could introduce hyperemia artifacts through mechanical or chemical irritation. Second, regional hair follicle cycling could contribute to some of the hyperemic response as angiogenesis is activated during the anagen phase of hair follicle development (24). Third, PMA is known to be an inducer of acute inflammation. Thus, we felt that this model had too many confounding variables for adequate analysis of EIBS.

UVB exposure represents the primary etiologic agent for nonmelanoma skin cancer (NMSC) formation (25). We therefore switched to a mouse model of photocarcinogenesis using hairless, albino SKH-1 mice (26). SKH-1 mice exhibit a defect in hair cycling in which the hair follicles permanently arrest in catagen phase (26). Thus, the permanent hair loss makes this mouse more suitable for both imaging and UVB-irradiation studies, whereas the lack of hair cycling through anagen provides a better model for studies on dermal angiogenesis. Figure 2A illustrates a typical regional pattern of dermal Hb content in non-UVB–treated SKH-1 mice. The regional variability was marked by gradual changes in Hb content, with higher levels seen overlying the spinal hump, and generally showing a symmetrical pattern on either side of the spinal midline.

Downloaded from cancerres.aacrjournals.org on January 3, 2013
Copyright © 2013 American Association for Cancer Research

Published OnlineFirst October 29, 2012; DOI:10.1158/0008-5472.CAN-12-2670

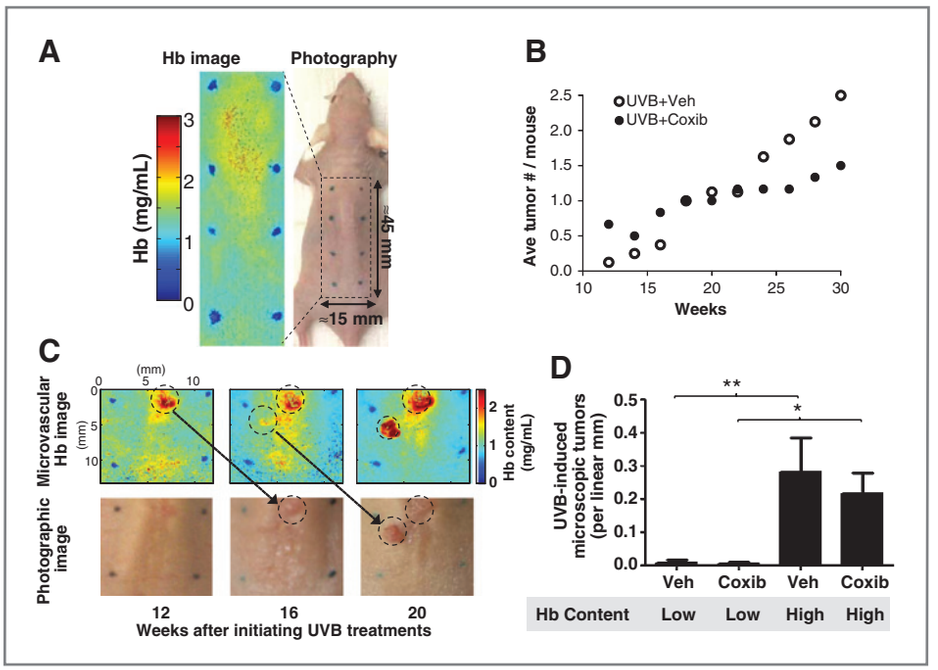


Figure 2. Focal areas of intense hyperemia precede tumor occurrence and serve to indicate sites at high risk for tumor development. A, color photographic image of an SKH-1 hairless mouse and the tattoo marks (blue) that were used to orient subsequent imaging studies. These tattoo marks are also visible in the Hb content image. B, celecoxib treatment suppresses tumor formation following UVB treatments. Tumor multiplicity in UVB-treated mice that were also treated with vehicle (Veh) or celecoxib (Coxib) were calculated as the average number of tumors per mouse. C, Hb content images and the corresponding photographs are shown for a representative mouse at 12, 16, and 20 weeks after initiating UVB treatments. Focal areas of increased hyperemia are noted to appear before visible tumor appearance (hashed circles). D, after the final imaging study (30 weeks after initiating UVB treatments), the irradiated mice were euthanized and skin free of visible tumors was excised from areas of low and high Hb content. Histopathologic assessment for the presence of small tumors visible microscopically was then done. Total microscopic tumors were normalized to the mean tissue section length for each mouse. The data show the mean tumor density per linear mm in areas of low and high Hb content for both Veh- and Coxib-treated animals. Tumors/section length (mm) were significantly higher in areas of high Hb content relative to low Hb content for both Veh-treated (**, $P = 0.0097$ for a Mann–Whitney U test) and for Coxib-treated animals (*, $P = 0.0436$ for a Mann–Whitney U test).

For our UVB studies, we also wished to avoid the influence of UVB-induced acute inflammation (sunburn); thus, a cumulative carcinogenic dose of UVB was administered by repetitive UVB irradiations over the first 10 weeks and then discontinued (21). Examining the Hb content beginning 2 weeks after cessation of UVB dosing allowed us to examine changes in blood supply at the time when tumors initially began to appear in this mouse model (19, 20), but after the acute sunburn effect had resolved. This also mimics human behavior, in which sun-avoidance strategies are often used only after significant cutaneous photodamage is apparent or a first tumor is found.

In Fig. 2B, we show that 10 weeks of UVB treatment resulted in grossly visible tumor formation starting 2 weeks after discontinuing UVB treatments. As expected, peak tumor multiplicity was suppressed by 40% in the celecoxib-treated mice. We also noted that tumor-associated hyperemia is easily visualized using our bioimaging approach as markedly elevated Hb content with sharply demarcated borders that tend to outline the tumor margins (Fig. 2C). Indeed, focal hyperemia associated with tumors was seen to resolve in tumors that spontaneously disappeared (Supplementary Fig. S4). Importantly, as in the 9 tumors seen in the DMBA/PMA studies, all 25 visually apparent tumors that occurred in our photocarcinogenesis studies were preceded by focal areas of increased hyperemia (Fig. 2C). These hyperemic foci either persisted after resolution of the acute UVB-induced erythema reaction, or began to appear within the early weeks after UVB cessation.

While the earlier studies showed that all visible tumors developed in smaller areas of the epidermis characterized by focal hyperemia, not all areas of hyperemia were seen to develop visibly apparent tumors. We therefore euthanized the mice 20 weeks after stopping UVB treatments and biopsied skin from areas of high and low Hb content that did not contain a grossly visible tumor. After histopathologic examination of H&E–stained sections, a number of papillomas and microinvasive squamous cell carcinomas were observed that were too small to be seen by visual inspection of the skin (Fig. 2D and Supplementary Table S1). Of 34 microscopically observed tumors seen in irradiated vehicle- or celecoxib-treated skin, 32 tumors occurred in areas of high Hb content. Thus, a total of 57 tumors (25 large visible tumors and 32 microscopic tumors) were seen in the much smaller areas of skin exhibiting hyperemia, whereas only 2 microscopically observed papillomas were seen in the much larger area of skin without hyperemia. Interestingly, celecoxib did not cause a significant change in the average numbers of microscopically observed tumors within the existing areas of hyperemia (Fig. 2D).

Downloaded from cancerres.aacrjournals.org on January 3, 2013
Copyright © 2013 American Association for Cancer Research

Published OnlineFirst October 29, 2012; DOI:10.1158/0008-5472.CAN-12-2670

Celecoxib's chemopreventive activity correlates with its ability to suppress the area of treated skin that exhibits focal hyperemia rather than a global suppression of Hb content

In Fig. 3A, we contrast the typical regional pattern of Hb content in nonirradiated mouse skin with the Hb content map of a mouse 6 weeks after stopping UVB treatments. Compared with the symmetrical and gradual changes in Hb content noted in nonirradiated mice, mice treated with a carcinogenic dose of UVB showed a nonsymmetrical distribution, with focal areas of high Hb content exhibiting distinct borders and an abrupt transition to intense hyperemia. Importantly, areas surrounding these focal hyperemic areas often exhibited lower Hb content than nonirradiated mice (more blue coloration). On the basis of this focal pattern of intense hyperemia, we felt that overall averaged Hb content from the entire imaging failed to adequately assess either the Hb distribution pattern or tumor risk. It was therefore not particularly surprising that there was actually a modest and significant decrease in overall Hb content in UVB-treated skin relative to nonirradiated mice when the Hb content was averaged over the entire imaging area (Supplementary Fig. S5). Moreover, in celecoxib-treated mice, overall Hb content failed to show any correlation with celecoxib's chemopreventive activity (Supplementary Fig. S5).

Insofar, as averaged Hb over the entire imaging area did not seem to adequately assess the changes in hyperemia that we were observing in irradiated mice after cessation of UVB treatments, we therefore used a different analytic approach that took into account the highly focal and heterogeneous pattern of Hb content distribution. We first prepared a threshold map of hyperemic areas that had Hb content greater than 1.6 mg/mL similar to that seen in Fig. 1C. When Hb content was measured only in these smaller foci of intense hyperemia (Fig. 3B), we now saw that UVB treatment did indeed increase the amount of Hb present within the hyperemic foci. Thus, the data supported our conclusion that hyperemic areas that persist following cessation of UVB treatments represented focal areas of more intense hyperemia than that observed with normal regional blood flow. Interestingly, as with the tumor data in Fig. 2D, the Hb content within these hyperemic foci failed to correlate with the chemopreventive activity of celecoxib (Fig. 3B).

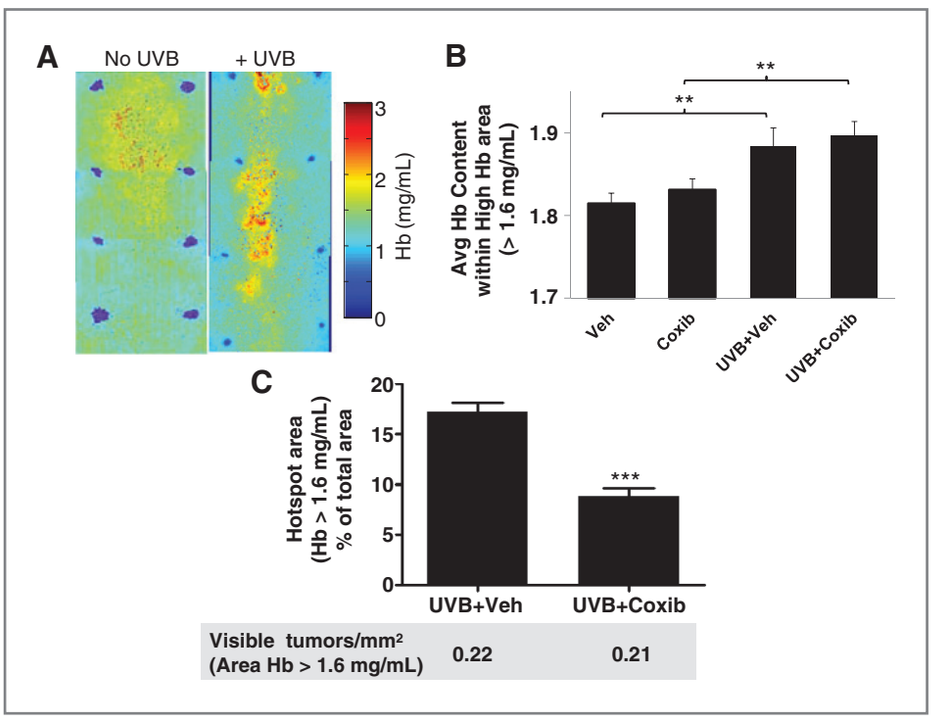


Figure 3. UVB-induced hyperemic foci contain higher Hb content than areas of high regional blood flow in nonirradiated animals, whereas celecoxib's chemopreventive activity is associated with a reduction in the area of hyperemic foci. A, representative Hb content maps are shown for the dorsal surface of a nonirradiated SKH-1 mouse and a mouse 6 weeks after cessation of UVB treatments. B, beginning 2 weeks after stopping UVB treatments, threshold maps were obtained at 2 week intervals for areas with Hb content more than 1.6 mg/mL. The average Hb content within the 1.6 mg/mL threshold mapped sites was determined for each mouse at each time point. The time (12–28 weeks) averaged mean and SD is shown for each treatment condition. The differences between UVB-irradiated and sham-irradiated groups were statistically significant (**, $P = 0.0032$ for Veh and UVB+Veh and **, $P = 0.0073$ for Coxib and UVB+Coxib). C, after threshold mapping, the percentage of the imaging area containing Hb greater than 1.6 mg/mL is shown as a time (12–28 weeks) averaged mean and a SD for all animals (5 or 8 animals per treatment group). Celecoxib treatment results in a statistically significant reduction in the total area of involved skin with Hb content more than 1.6 mg/mL ($P = 0.0002$ for a Mann–Whitney U test). Note that all visible tumors seen in the imaging area occurred in areas of preexisting hyperemia. Visible tumor occurrence after normalizing to the percentage of the imaging area with Hb content more than 1.6 mg/mL is shown below the plot (***, $P = 0.0002$ for a Mann–Whitney U test).

Downloaded from cancerres.aacrjournals.org on January 3, 2013
Copyright © 2013 American Association for Cancer Research

Published OnlineFirst October 29, 2012; DOI:10.1158/0008-5472.CAN-12-2670

In the earlier studies, we show that tumors almost invariably occur in small focal areas of intense hyperemia. However, neither the intensity of Hb content within these areas nor the tumor burden is altered by a chemopreventive dose of celecoxib. We therefore hypothesized that if celecoxib treatment does not reduce tumor risk within these foci, perhaps it reduces tumorigenesis by suppressing the total area of involved skin at risk for tumor formation. In Fig. 3C, we show that celecoxib treatment results in a suppression of the total imaging area exhibiting hyperemic foci formation by 49.1% (areas with Hb content > 1.6 mg/mL were 10.3% and 5.5% of the imaging area for vehicle- and celecoxib-treated animals, respectively). This reduction in the area at risk for tumor formation correlates well with celecoxib's chemopreventive activity (Fig. 2B; refs. 20, 21) As expected on the basis of the data in Fig. 2D, we show an essentially identical rate of visible tumor formation within the hyperemic areas that persist in both vehicle- and celecoxib-treated mice (0.22 and 0.21 tumors/mm^2).

Areas of focal hyperemia not only persist in the absence of a visible tumor, but also expand following cessation of UVB treatment

As noted earlier, after discontinuing UVB treatments, areas of increased hyperemia were detected that persisted or formed over the ensuing weeks and months. Interestingly, an examination of Hb content images revealed that these persistent areas of focal hyperemia seemed to expand over time (Fig. 4A). To assess this quantitatively, we generated threshold maps of Hb content more than 1.6 mg/mL, measured the total area of skin exhibiting Hb content above this threshold, and plotted the data at 2-week intervals after stopping UVB irradiations (Fig. 4B). As expected, UVB-irradiated mice treated with both vehicle and celecoxib showed an increase in the area of hyperemic foci over time. In addition, the expansion of hyperemic areas was seen to precede grossly observable tumor formation (Fig. 4C). As in Fig. 3C, celecoxib treatment suppressed the overall area of skin with high Hb content at each imaging time point (Fig. 4B and C).

Hyperemic foci correspond to areas of angiogenesis

In studies by others in rat colon, azoxymethane-induced EIBS corresponded with increased angiogenesis (6). We therefore examined whether hyperemic foci exhibited evidence of angiogenesis. In Fig. 5A–D, we show the histologic differences in skin sections obtained from nontumor-bearing areas of high and low Hb content 20 weeks after stopping UVB treatments. Following H&E staining, we observed that areas of high Hb content in UVB-irradiated skin exhibited marked epidermal

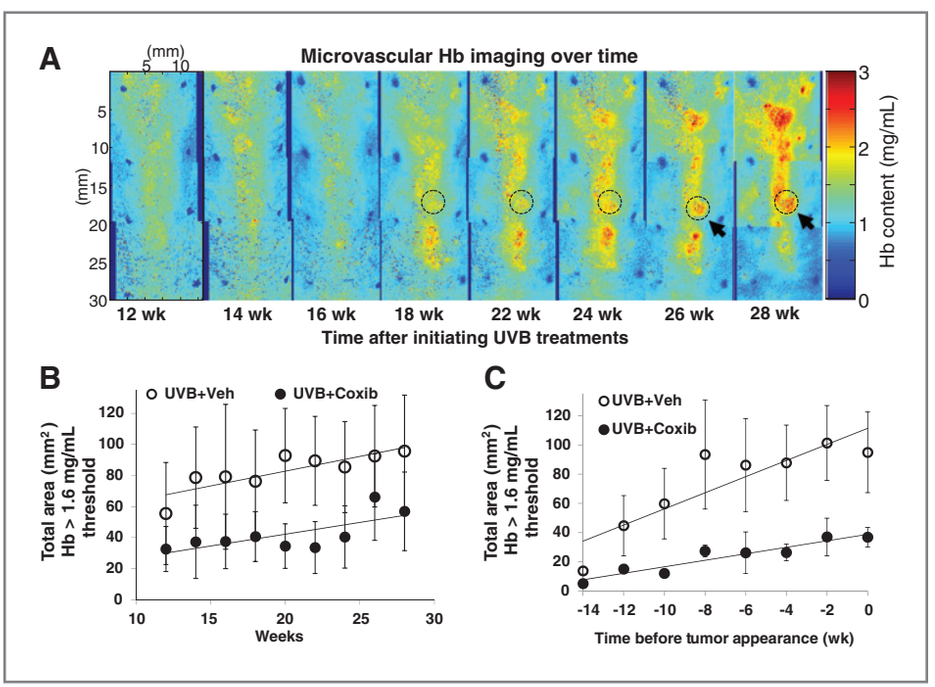


Figure 4. UVB-induced hyperemic foci expand following cessation of carcinogenic UVB treatments. A, representative microvascular Hb content maps from a single UVB-treated mouse at biweekly intervals after cessation of UVB treatments reveal the spatial and temporal extent of focal hyperemia. Note that hyperemic foci not only persist, but also expand in size leading up to tumor formation. The hashed circles indicate a hyperemic foci that preceded the appearance of a tumor that became visible in week 26 and 28 (arrows). B, after threshold mapping for areas with Hb content more than 1.6 mg/mL, the mean area of hyperemic foci was calculated. The areas of high Hb content expanded after cessation of UVB treatment in both UVB-treated mice ($P = 0.005$ for the slope estimate over time in UVB+Veh animals and $P = 0.029$ in UVB+Coxib mice). The overall difference of focal hyperemic area between the Veh- and Coxib-treated groups was statistically significant ($P = 0.044$). However, the slope estimates between the 2 groups were not statistically different. C, expanding areas of focally high Hb content were observed in the weeks preceding visible tumor appearance. The slope estimates of the linear regression for both groups were significant ($P = 0.004$ for UVB+Veh and $P = 0$ for UVB+Coxib). The difference in the slopes between the 2 groups was statistically significant ($P = 0.021$).

Downloaded from cancerres.aacrjournals.org on January 3, 2013
Copyright © 2013 American Association for Cancer Research

Published OnlineFirst October 29, 2012; DOI:10.1158/0008-5472.CAN-12-2670

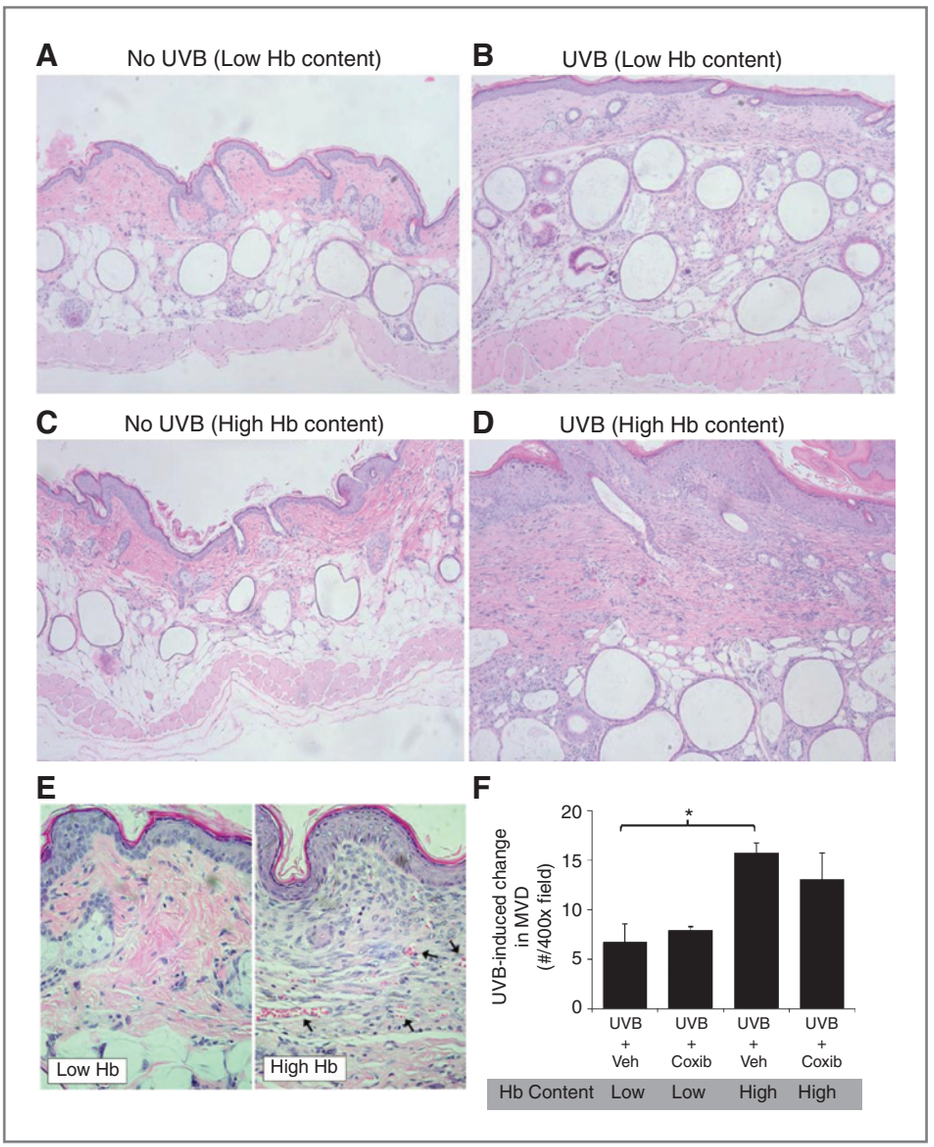


Figure 5. Focal areas of persistent hyperemia exhibit epidermal hyperplasia, the presence of dermal inflammatory infiltrates, and increased microvessel density 20 weeks after stopping UVB irradiations. A–D, representative low power photomicrographs of H&E–stained sections from: A, area of low Hb content in nonirradiated mouse skin. B, area of low Hb content in irradiated mouse skin. C, area of high Hb content from nonirradiated skin. D, area of high Hb content from irradiated skin. E, representative high power photomicrograph showing H&E–stained areas of both low and high Hb content. Note the hypercellular dermis with increased small vessels containing erythrocytes (arrows) in the area of high Hb content. F, immunohistochemical labeling for the endothelial marker CD31 and MVD determination was conducted. Non-UVB–treated mice showed no significant difference between areas of high and low regional blood flow or between Veh or Coxib treatment. After subtracting the baseline MVD from the relative nonirradiated control group, the increase in MVD was plotted as the mean and SD ($n = 4$ mice for Veh and $n = 3$ mice for Coxib treatment). A significant difference was noted between the areas of high and low Hb content for the UVB+Veh treated mice ($P = 0.0209$ for a Mann–Whitney U test).

hyperplasia, a hypercellular dermis consistent with increased inflammatory cell infiltrates and increased numbers of small vessels (Fig. 5D and E). In contrast, irradiated skin obtained from areas of low Hb content were largely normal, with some focal areas of mild epidermal hyperplasia and a variable but generally mild increase in dermal hypercellularity (Fig. 5B). In contrast, in nonirradiated control mice there was no apparent histologic change in areas of high and low regional blood flow (Fig. 5A and C). To verify that focal hyperemia was associated with increased angiogenesis in irradiated mice, we assessed MVD. In Fig. 5F, we show that MVD was significantly greater in areas of high Hb content in UVB-treated mice compared with areas of low Hb content. Celecoxib treatment also had no significant effect on MVD in the smaller hyperemic areas that persisted despite celecoxib treatment. However, this was expected as we had already shown that celecoxib had no significant effect on Hb content within hyperemic foci (Fig. 3B).

UVB-induced acute erythema reactions (sunburn) are uninformative about future tumorigenesis or the chemopreventive efficacy of celecoxib

Our photocarcinogenesis studies were designed to remove potential interference from UVB-induced acute hyperemia. As we expected, a marked increase in Hb content was observed using our imaging approach in UVB-irradiated mice 72 hours after the final irradiation (Fig. 6A, top left). This increase in Hb content was also visually apparent as an area of erythema (sunburn) in the photographic image (Fig. 6A, bottom left). Importantly, within a few weeks after discontinuing UVB treatments, visible erythema disappeared and was accompanied by a return to a largely normal pattern of regional Hb content (Fig. 6A, top right). It is also important to note that transient UVB-induced hyperemia failed to correlate with sites of eventual tumor formation (Fig. 6A, hashed circle). Nor did visible erythema reactions correlate with the chemopreventive

Downloaded from cancerres.aacrjournals.org on January 3, 2013
Copyright © 2013 American Association for Cancer Research

Published OnlineFirst October 29, 2012; DOI:10.1158/0008-5472.CAN-12-2670

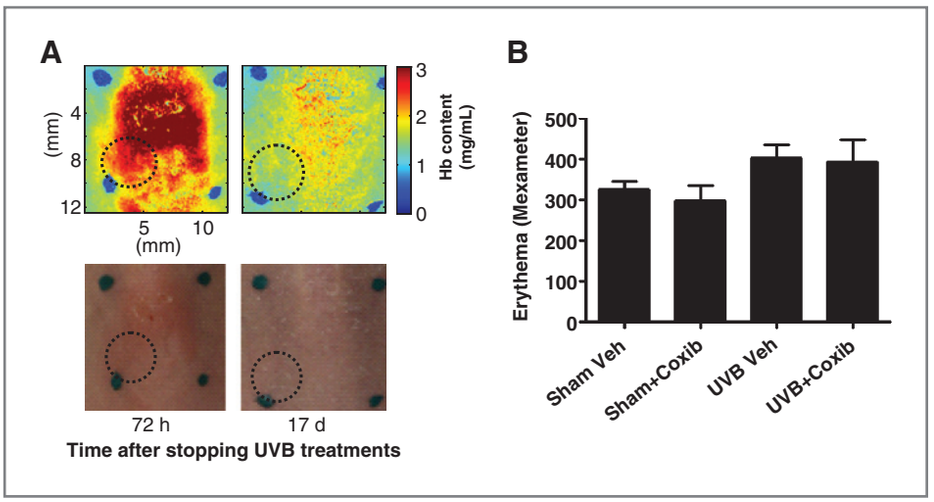


Figure 6. Neither clinically apparent erythema (sunburn) nor averaged subclinical Hb content predict the site of future tumor formation or the chemopreventive activity of celecoxib. A, representative microvascular Hb content images (top) and photographic images (bottom) are shown showing the intense hyperemia (top) and erythema (bottom) that is still evident 72 hours after the final UVB dose. A Hb content image and photographic image of the same site 17 days later show resolution of the acute hyperemia and erythema response. Acute hyperemia did not correlate with the future appearance of tumors. The dashed circles indicate a site of a tumor that appeared 10 weeks after stopping UVB treatments. B, erythema was measured using a narrow-band reflectance spectrophotometer (Mexameter) in the fifth week of UVB treatments (72 hours after the previous UVB dose; $P = 0.0515$ for a Kruskal–Wallis test). Results represent the mean ± SD of the erythema measurements ($n = 2$ nonirradiated and 5–6 irradiated mice per group).

activity of celecoxib. This subjective assessment was verified by measuring the acute UVB-induced erythema reaction using a narrow-band reflectance spectrophotometer (Mexameter; Fig. 6B; see Supplementary Methods).

Discussion

Field cancerization is clearly present in human nonmelanoma skin cancer, in which field treatments are often necessary to treat multiple premalignant actinic lesions that occur on sun-damaged skin (27). Multiple theories have been proposed to explain how a cancerization field develops (3, 28). However, it is difficult to firmly establish the nature of early field development when the field cannot be visualized before grossly visible tumor formation. In our study, we provide multiple lines of evidence that hyperemia is an early marker of field cancerization and that our imaging approach visualizes the cancerization field in experimental cutaneous murine carcinogenesis: (i) tumors almost invariably formed in areas of focal hyperemia that persist long after the cessation of carcinogenic UVB exposures. (ii) Hyperemic areas in which tumors formed represented a minor fraction of the total treated area and were multifocal in nature. (iii) The ability of celecoxib to suppress tumor formation correlated well with its ability to suppress the area of UVB-treated skin that exhibited high Hb content. (iv) Hyperemic foci not only persisted, but also expanded in size long after cessation of UVB treatments. Moreover, expansion was seen to precede the appearance of a grossly visible tumor. (v) Hyperemic foci in areas where no tumor were present had characteristic early-histologic changes associated with tumorigenesis, including epidermal hyperplasia, increased dermal hypercellularity suggestive of an inflammatory infiltrate, and increased angiogenesis. Importantly, these histologic changes were observed even though the tissue was removed long after UVB irradiations had stopped (20 weeks), indicating a mechanism for sustaining the epidermal hyperplasia and angiogenesis.

Our observation that both hyperemic foci and tumor risk are not homogenously distributed but rather are limited to a small heterogeneous segment of the entire carcinogen-treated surface is important. Our methodology could potentially allow investigators to actually visualize this multifocal "field" to allow targeted biopsies to assess locoregional changes associated with early events in carcinogenesis, and could provide a method to assess the efficacy of chemopreventive agents. Moreover, the ability to target sites at high risk for tumor formation for longitudinal studies in live animals will provide important information about the early premalignant changes that are specific to the cancerization field. Our methodology would be of particular importance if validated in human studies, such as individuals with significant cutaneous photodamage or early premalignant actinic disease that are at high risk for nonmelanoma skin cancer formation. Currently, studies in live volunteers are constrained by the limited amounts of tissue that can be ethically obtained. High variability due to sampling bias results in the need for high numbers of volunteers to obtain statistically valid data or restricts studies to sites of visible premalignant or malignant lesions.

Studies of carcinogen-induced malignancy in skin and other tissues indicates that the angiogenic switch can be triggered much earlier during the carcinogenic sequence, occurring as early as the sustained hyperplastic response (7, 29). This differs somewhat from the classic model of tumor-induced angiogenesis, in which an existing avascular tumor switches on proangiogenic signals that provide the increased blood supply needed for tumor expansion and progression (7, 29). However, this classic model of an "angiogenic switch" is generally

Downloaded from cancerres.aacrjournals.org on January 3, 2013
Copyright © 2013 American Association for Cancer Research

Published OnlineFirst October 29, 2012; DOI:10.1158/0008-5472.CAN-12-2670

observed with the use of various oncogene-driven mouse models (29). Thus, our findings support the idea that the angiogenic switch occurs very early during cutaneous carcinogenesis rather than the classic model, whereby the angiogenic switch occurs later in existing avascular visible tumors. However, further studies are necessary in our model to verify that angiogenesis is responsible for the hyperemic foci present before the time when tumors are evident.

One of the interesting findings of our study is that celecoxib's chemopreventive activity correlates directly with its ability to decrease the total surface area exhibiting hyperemic foci. In contrast, celecoxib failed to suppress either tumor formation or the intensity of the hyperemia within these foci. A number of possible explanations could explain these observations, all of which would require further studies to verify. One hypothesis would be that the hyperemic foci represent patches of proliferating (pre)malignant keratinocytes that produce the proangiogenic cytokines necessary to trigger increased dermal blood supply. COX-2 inhibitors exhibit potent effects on the growth and survival of normal and neoplastic epidermal keratinocytes (30, 31). Thus, celecoxib treatment could limit the clonal expansion of these (pre)malignant epidermal patches, thus limiting their size. Alternatively, COX-2 inhibitors are known to suppress UVB-induced inflammation and this is closely associated with their antineoplastic activity (21, 26). Moreover, a persistent inflammatory stromal environment is associated with both angiogenesis and increased overlying epithelial tumor development (9, 10, 32). Thus, it is possible that celecoxib suppresses the formation of persistent inflammatory foci, which in turn suppress angiogenesis and overlying tumor development. In this case, it is unclear why some hyperemic foci are resistant to the effects of celecoxib. A trivial explanation would be that these areas failed to receive adequate levels of celecoxib due to variable topical delivery. However, this seems highly unlikely given that each mouse was treated on multiple occasions over the 30-week course of the study. Still, repeating these studies using systemic delivery of celecoxib would be of interest.

The risk of tumor development is well known to persist for years after the removal of carcinogenic insults. A number of theories have been advanced to explain these observations. This includes dormant tumors that are induced to progress due to an angiogenic switch that triggers increased blood supply (29) or the acquisition of proliferative self-sufficiency or survival advantage mediated by mutagenic events or a nurturing microenvironment (8, 33). Unfortunately, the inability to specifically identify tissue sites at the earliest stages of tumorigenesis limits the ability to define why risk for tumor development persists. Our data suggest that an unknown mechanism exists that sustains and actually expands areas of focal hyperemia after removal of a carcinogenic insult. As mentioned earlier, this could be due to continued clonal expansion of (pre)malignant patches or possibly the presence of inflammatory feedback loops driving persistent inflammatory angiogenesis. Identifying the engine that drives the persistence and expansion of these hyperemic zones could provide answers to how risk for tumor formation persists in individuals who undertake risk-avoidance behavioral changes.

Disclosure of Potential Conflicts of Interest

R. Konger, Z. Xu, and Y.L. Kim have ownership in a Provisional Patent Application. No potential conflicts of interest were disclosed by the other authors.

Authors' Contributions

Conception and design: R.L. Konger, S.J. Warren, Y.L. Kim
Development of methodology: R.L. Konger, Z. Xu, R.P. Sahu, S.J. Warren, Y.L. Kim
Acquisition of data (provided animals, acquired and managed patients, provided facilities, etc.): Z. Xu, B.M. Rashid, S.R. Mehta, D.R. Mohamed, S.C. DaSilva-Arnold, S.J. Warren, Y.L. Kim
Analysis and interpretation of data (e.g., statistical analysis, biostatistics, computational analysis): R.L. Konger, Z. Xu, D.R. Mohamed, J.R. Bradish, S.J. Warren, Y.L. Kim
Writing, review, and/or revision of the manuscript: R.L. Konger, J.R. Bradish, Y.L. Kim
Administrative, technical, or material support (i.e., reporting or organizing data, constructing databases): R.L. Konger, Z. Xu, R.P. Sahu, B.M. Rashid, S.R. Mehta, D.R. Mohamed, Y.L. Kim
Study supervision: R.L. Konger, B.M. Rashid, Y.L. Kim

Acknowledgments

The authors thank Dr. Jeffrey Travers for his insights and editorial commentary.

Grant Support

This study was supported by the funding from the NIH: R01HL062996, R21ES017497, R03AR053710, and R25CA128770.

The costs of publication of this article were defrayed in part by the payment of page charges. This article must therefore be hereby marked *advertisement* in accordance with 18 U.S.C. Section 1734 solely to indicate this fact.

Received July 5, 2012; revised October 16, 2012; accepted October 17, 2012; published OnlineFirst October 29, 2012.

References

1. Slaughter DP, Southwick HW, Smejkal W. Field cancerization in oral stratified squamous epithelium; clinical implications of multicentric origin. Cancer 1953;6:963–8.
2. Dakubo G, Jakupciak J, Birch-Machin M, Parr R. Clinical implications and utility of field cancerization. Cancer Cell Int 2007;7:2.
3. van Oijen MGCT, Slootweg PJ. Oral field cancerization: carcinogen-induced independent events or micrometastatic deposits? Cancer Epidemiol Biomarkers Prev 2000;9:249–56.
4. Wali RK, Roy HK, Kim YL, Liu Y, Koetsier JL, Kunte DP, et al. Increased microvascular blood content is an early event in colon carcinogenesis. Gut 2005;54:654–60.
5. Gomes AJ, Roy HK, Turzhitsky V, Kim Y, Rogers JD, Ruderman S, et al. Rectal mucosal microvascular blood supply increase is associated with colonic neoplasia. Clin Cancer Res 2009;15:3110–7.
6. Tiwari AK, Crawford SE, Radosevich A, Wali RK, Stypula Y, Kunte DP, et al. Neo-angiogenesis and the premalignant micro-circulatory augmentation of early colon carcinogenesis. Cancer Lett 2011;306:205–13.
7. Hanahan D, Folkman J. Patterns and emerging mechanisms of the angiogenic switch during tumorigenesis. Cell 1996;86:353–64.
8. Spencer SL, Gerety RA, Pienta KJ, Forrest S. Modeling somatic evolution in tumorigenesis. Plos Comput Biol 2006;2:939–47.
9. Hanahan D, Weinberg Robert A. Hallmarks of cancer: the next generation. Cell 2011;144:646–74.
10. Albini A, Tosetti F, Benelli R, Noonan DM. Tumor inflammatory angiogenesis and its chemoprevention. Cancer Res 2005;65:10637–41.

Downloaded from cancerres.aacrjournals.org on January 3, 2013
Copyright © 2013 American Association for Cancer Research

Published OnlineFirst October 29, 2012; DOI:10.1158/0008-5472.CAN-12-2670

11. Abulafia O, Triest WE, Sherer DM. Angiogenesis in squamous cell carcinoma *in situ* and microinvasive carcinoma of the uterine cervix. Obstet Gynecol 1996;88:927–32.
12. Erez N, Truitt M, Olson P, Hanahan D. Cancer-associated fibroblasts are activated in incipient neoplasia to orchestrate tumor-promoting inflammation in an NF-κB-dependent manner. Cancer Cell 2010;17: 135–47.
13. Irigaray P, Newby JA, Clapp R, Hardell L, Howard V, Montagnier L, et al. Lifestyle-related factors and environmental agents causing cancer: an overview. Biomed Pharmacother 2007;61:640–58.
14. Anand P, Kunnumakara A, Sundaram C, Harikumar K, Tharakan S, Lai O, et al. Cancer is a preventable disease that requires major lifestyle changes. Pharm Res 2008;25:2097–116.
15. Lichtenstein P, Holm NV, Verkasalo PK, Iliadou A, Kaprio J, Koskenvuo M, et al. Environmental and heritable factors in the causation of cancer—analyses of cohorts of twins from sweden, denmark, and finland. N Engl J Med 2000;343:78–85.
16. Balkwill F, Charles KA, Mantovani A. Smoldering and polarized inflammation in the initiation and promotion of malignant disease. Cancer Cell 2005;7:211–7.
17. Harris RE. Cyclooxygenase-2 (cox-2) and the inflammogenesis of cancer. Subcell Biochem 2007;42:93–126.
18. Liu J, Xu Z, Song Q, Konger RL, Kim YL. Enhancement factor in low-coherence enhanced backscattering and its applications for characterizing experimental skin carcinogenesis. J Biomed Opt 2010;15: 037011.
19. Sahu RP, Dasilva SC, Rashid B, Martel KC, Jernigan D, Mehta SR, et al. Mice lacking epidermal PPARγ exhibit a marked augmentation in photocarcinogenesis associated with increased UVB-induced apoptosis, inflammation and barrier dysfunction. Int J Cancer 2012;131: E1055–66
20. Wilgus TA, Koki AT, Zweifel BS, Kusewitt DF, Rubal PA, Oberyszyn TM. Inhibition of cutaneous ultraviolet light b-mediated inflammation and tumor formation with topical celecoxib treatment. Mol Carcinog 2003; 38:49–58.
21. Pentland AP, Schoggins JW, Scott GA, Khan KN, Han R. Reduction of UV-induced skin tumors in hairless mice by selective cox-2 inhibition. Carcinogenesis 1999;20:1939–44.
22. Xu Z, Liu J, Hong DH, Nguyen VQ, Kim MR, Mohammed SI, et al. Back-directional gated spectroscopic imaging for diffuse light suppression in high anisotropic media and its preclinical applications for microvascular imaging. IEEE J Sel Top Quant Electron 2010;16: 815–23.
23. Xu Z, Liu J, Kim YL. Diffuse light suppression of back-directional gating imaging in high anisotropic media. J Biomed Opt 2009;14:030510.
24. Mecklenburg L, Tobin DJ, Muller-Rover S, Handjiski B, Wendt G, Peters EMJ, et al. Active hair growth (anagen) is associated with angiogenesis. J Invest Dermatol 2000;114:909–16.
25. Elmets CA, Viner JL, Pentland AP, Cantrell W, Lin HY, Bailey H, et al. Chemoprevention of nonmelanoma skin cancer with celecoxib: a randomized, double-blind, placebo-controlled trial. J Natl Cancer Inst 2010;102:1835–44.
26. Benavides F, Oberyszyn TM, VanBuskirk AM, Reeve VE, Kusewitt DF. The hairless mouse in skin research. J Dermatol Sci 2009;53:10–8.
27. Askew DA, Mickan SM, Soyer HP, Wilkinson D. Effectiveness of 5-fluorouracil treatment for actinic keratosis—a systematic review of randomized controlled trials. Intl J Dermatol 2009;48: 453–63.
28. Braakhuis BJM, Tabor MP, Kummer JA, Leemans CR, Brakenhoff RH. A genetic explanation of slaughter's concept of field cancerization. Cancer Res 2003;63:1727–30.
29. Bergers G, Benjamin LE. Tumorigenesis and the angiogenic switch. Nat Rev Cancer 2003;3:401–10.
30. Ansari KM, Rundhaug JE, Fischer SM. Multiple signaling pathways are responsible for prostaglandin e-2-induced murine keratinocyte proliferation. Mol Cancer Res 2008;6:1003–16.
31. Tripp CS, Blomme EAG, Chinn KS, Hardy MM, LaCelle P, Pentland AP. Epidermal cox-2 induction following ultraviolet irradiation: suggested mechanism for the role of cox-2 inhibition in photoprotection. J Invest Dermatol 2003;121:853–61.
32. Hatton JL, Parent A, Tober KL, Hoppes T, Wulff BC, Duncan FJ, et al. Depletion of CD4+ cells exacerbates the cutaneous response to acute and chronic UVB exposure. J Invest Dermatol 2007;127: 1507–15.
33. Hanahan D, Weinberg RA. The hallmarks of cancer. Cell 2000;100: 57–70.

Downloaded from cancerres.aacrjournals.org on January 3, 2013
Copyright © 2013 American Association for Cancer Research

SUPPLEMENTAL METHODS

Imaging platform. Utilizing our biophotometric imaging system (1, 2) (Fig S1), we visualized the spatial and temporal extent of detailed microvascular Hgb content in an area of 15 mm × 15 mm with a pixel size of 50 μm. By imaging adjacent fields and digitally merging the images, we extended the size of the field to approximately 15 mm × 45 mm. Our imaging technology is based on the combination of a back-directional gated filter and a spectral analysis: To remove a significant amount of unwanted diffuse light, back-directional (i.e. angular) gating in the detection part was implemented, because diffused light from tissue deviates from its original incident direction. In particular, back-directional gating allows the high anisotropic property of biological tissue to act as a waveguide and thus avascular tissue can become relatively transparent (2). Our biophotometric imaging system also provides a matrix of backscattered intensity as a function of x and y at each wavelength λ in the range of 400 – 750 nm. Thus, we can conduct a spectral analysis of intrinsic Hgb absorption to extract Hgb content in each (x, y) location (1).

Skin tissue phantom study. Because the spectral extraction of Hgb content and the imaging depth can be affected by the scattering properties of tissue, we measured the bulk scattering properties of the mouse skin using an integrating sphere method (3). We used excised mouse skin patches adjacent to the imaging area from 13 mice at several different time-points of tissue collection. The scattering pathlength of light in the skin l_s (i.e. averaged distance of one single scattering event) was 81.5 ± 12.5 (SD) μm and the anisotropy factor (i.e. average cosine of the scattering angle) was 0.84 ± 0.04. Note

that our spectral analysis assesses the total concentration of oxygenated and deoxygenated Hgb and it is relatively insensitive to the tissue anisotropy factor (1).

Imaging sensitivity, specificity and imaging depth. We utilized our earlier finding that the combination of a spectral analysis of endogenous Hgb absorption with diffuse-light-suppressed imaging increases the image resolution, contrast and penetration depth that are required to visualize microvasculature Hgb content (1, 2). Due to the high anisotropic light scattering properties of biological tissues, the use of back-directional gating removes unwanted diffuse light and improves the resolution and contrast of the reflected light for the spectral analysis of Hgb content (1, 2). To assess the imaging depth which the optical signal is averaged over, we measured the light backscattered from a tissue phantom without any absorbers as the optical thickness τ was varied from 0 to 90 ($\tau = 1$ means that the light traveling the medium undergoes one scattering event on average). Fig S2A shows that the backscattered intensity $I(\tau)$ first increases and then levels off with τ. We further determined the penetration depth by converting τ to a physical thickness T ($= \tau \times l_s$,). The data were fitted as $I(T) = 1 - \exp(-T/T_d)$, where T_d is the represented imaging depth when $I(T)$ reaches to $0.63 = \exp(-1)$. As shown in Fig S2B, T_d is 1.2 ± 0.2 mm in the range of l_s = 70 – 100 μm that we measured from the mouse skin using an integrating sphere method. Thus, the imaging depth of our biophotometric system covers the epidermis, the dermis, and the hypodermis of the mice.

We further determined the sensitivity and the precision of spectral Hgb quantitation using a series of phantom studies using microsphere suspensions and Hgb powders over the range of physiological Hgb concentration (Hgb = 0 - 3 mg/ml) and the scattering properties of the mouse skin (l_s = 70 - 100 μm). Fig S3A shows correlations between the actual Hgb concentration and the Hgb

absorption spectral area A, which are the summation of the difference between the model spectrum (without any Hgb) and the measured spectrum. The middle curve was used as the calibration curve to convert A to an absolute Hgb concentration in the unit of mg/ml. We defined the sensitivity S of Hgb quantitation as the derivative of A with respect to the actual Hgb concentration such that $S = dA/dHgb$. We also defined the precision P such that $P = (A_u - A_l)/A \times 100$ % at a given actual Hgb concentration, where A_u and A_l are the upper and lower calibration curves generated using $l_s = 70$ and 100 μm, respectively. As shown in Fig S3B & C, S decreases with the Hgb concentration, while P slightly increases with the Hgb concentration. Overall, S does not reach 0 and P is $< \sim 10$ % in the range of the optical properties of the mouse skin, supporting the idea that our spectral Hgb quantitation is highly reliable.

Visible erythema measurement. To quantitate the visible erythema reaction observed during UVB treatments and to evaluate the imaging approach in comparison to currently available methods, we utilized a standard clinically utilized narrow-band reflectance spectrophotometer (Mexameter®; Courage and Khazaka electronic GmbH, Köln, Germany) as described (4). This device is a simple probe-based method used clinically to quantitate "redness" in cutaneous lesions

Histopathologic tumor grading. The tumors were classified as papillomas (grades 1-3), microinvasive squamous cell carcinomas (MISCC) (stages 1-3), invasive squamous cell carcinomas, or anaplastic /spindle cell variants using the murine classification scheme of Benavides *et al* (5). Briefly, papillomas are tumors that lack evidence of stromal invasion, with grades 1-3 demonstrating an increasing papillar pattern and the presence of atypical cells at the base of dermal projections. Stage 1

MISCC showed definite invasion into the dermis but no invasion into the dermal fat layer while stage 2 MISCC had invasion into the dermal fat layer. Stage 3 MISCC showed invasion adjacent to but not into the panniculus carnosus. Invasive squamous cell carcinomas showed invasion into or through the panniculus carnosus. Tumor numbers obtained by histopathologic assessment were normalized to the linear length of each tissue section since tissue sections were notably larger for areas of low Hgb content.

Detailed statistical methods. Longitudinal data were analyzed using a two-stage analysis, in which multiple responses on each animal were reduced to single responses over time and then an analysis of variance (ANOVA) or a non-parametric equivalent of ANOVA were applied. In particular, to assess differences among several groups, Kruskal-Wallis tests were used as a non-parametric analysis. A Fisher's protected least-significant difference approach was used to adjust *p*-values for multiple comparisons. To compare two groups, a *t*-test or a Mann-Whitney *U* test were used. The assumptions (i.e. normality and uniform variance) for the parametric analyses were tested using a Shapiro-Wilks test and a Bartlett's test. Multiple linear regression analyses were used to evaluate slope estimates between Hgb variables and time including interaction and confounding terms of different groups and time. Statistical analyses were performed by using GraphPad Prism 5 (La Jolla, CA, USA) and Stata 9 (College Station, TX, USA).

SUPPLEMENTAL FIGURES

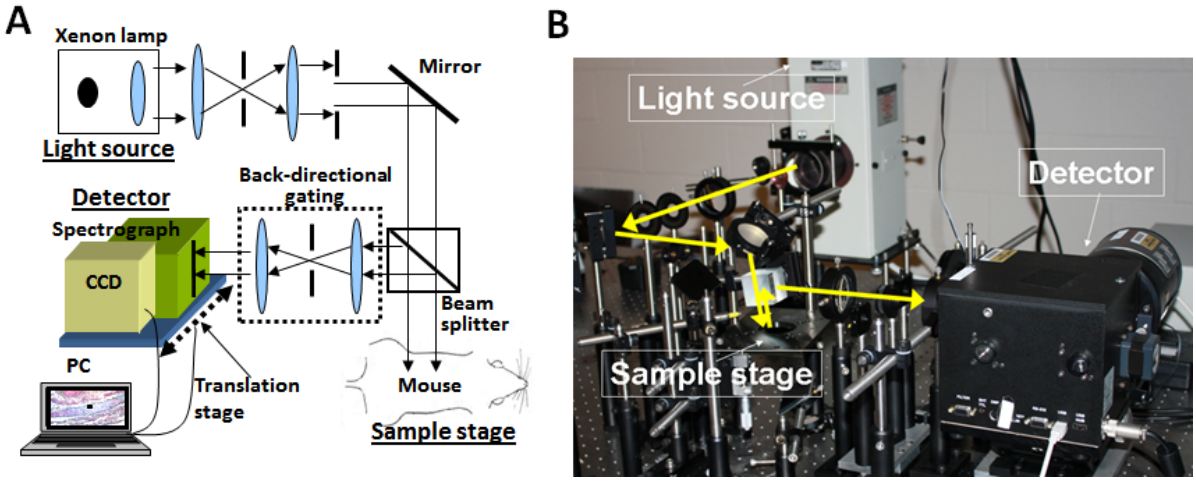


Figure S1: Imager setup. A) Our imaging method of combining Hgb spectral analysis with diffused-light-suppressed imaging serves as a simple mesoscopic method to sensitively and accurately quantify and spatially map Hgb content, bridging the gap between microscopic imaging (small field of view) and macroscopic imaging (low resolution). **B)** Photograph of the imaging setup.

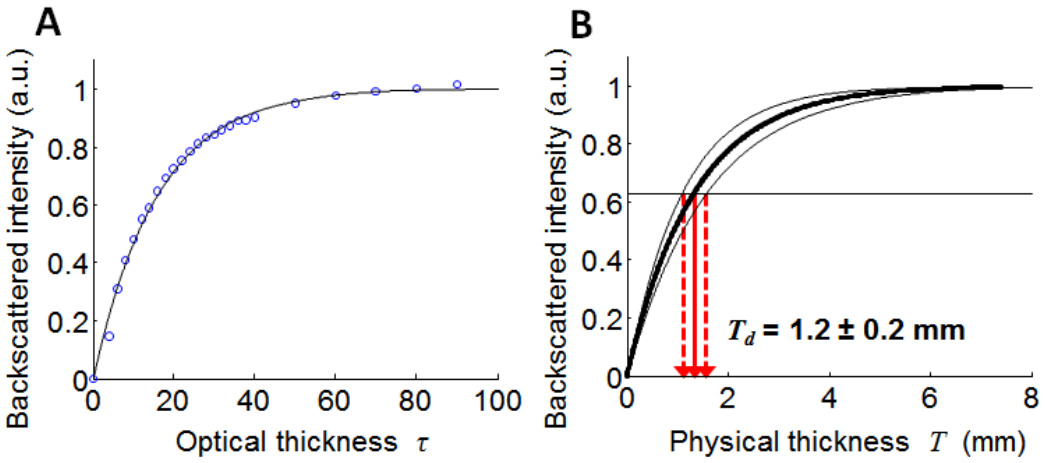


Figure S2: Imaging depth. A) The backscattered intensity as a function of the optical thickness τ. The line is the fitted curve using the exponential increase function as described in the text. The signal contribution is significantly reduced as τ increases. **B)** The backscattered intensity from the tissue phantom as the physical thickness T increases. The representative imaging depth $T_d = 1.2 \pm 0.2$ mm after the conversion of τ to T in the range of $l_s = 70$ - 100 µm.

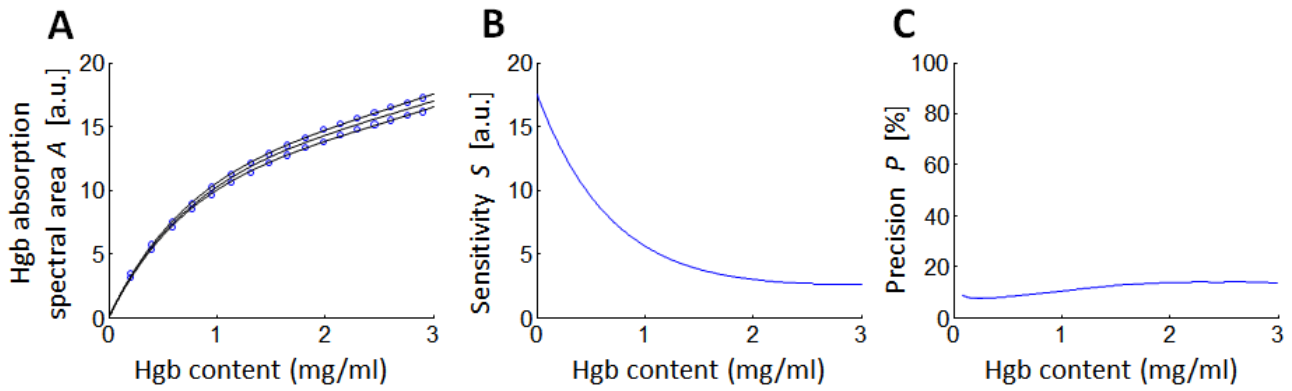


Figure S3: Hemoglobin (Hgb) quantitation. A) The Hgb absorption spectral area as the actual Hgb content increases in the range of l_s = 70 - 100 µm. The middle curve is used to convert to an absolute actual Hgb content. The upper and lower calibration curves are generated using tissue phantoms of l_s = 70 and 100 µm, respectively. **B)** The sensitivity S of the spectral Hgb quantitation as a function of Hgb content in the physical range of Hgb < 3 mg/ml**. C)** The precision P of the spectral Hgb quantitation as a function of Hgb content in the same physical range.

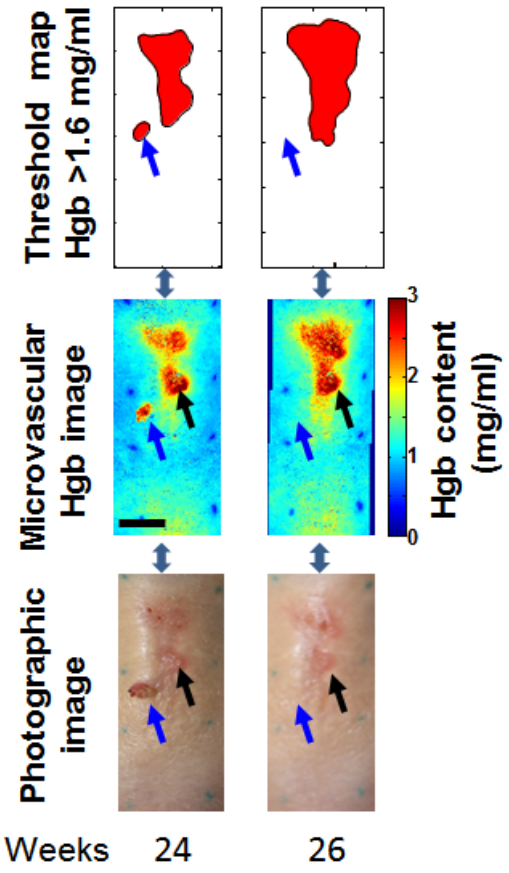


Figure S4: Tumor-induced angiogenesis is clearly visualized and is seen to disappear upon spontaneous loss of a tumor. Top panels) Threshold maps depicting the imaging area with > 1.6 mg/ml Hgb at 24 and 26 weeks after initiating UVB treatments (14 and 16 weeks after discontinuing UVB). **Middle panels)** Hgb color content maps. The scale bar = 5 mm. **Lower panels)** Photographic images of the imaged sites. The black arrows in each panel show the site of a visible tumor that was present at both time points. The blue arrows in each panel show the site of a visible tumor present at 24 weeks that was absent in the subsequent imaging study 2 weeks later. Of note, the hyperemic foci attributable to the tumor that spontaneously resolved were also seen to disappear.

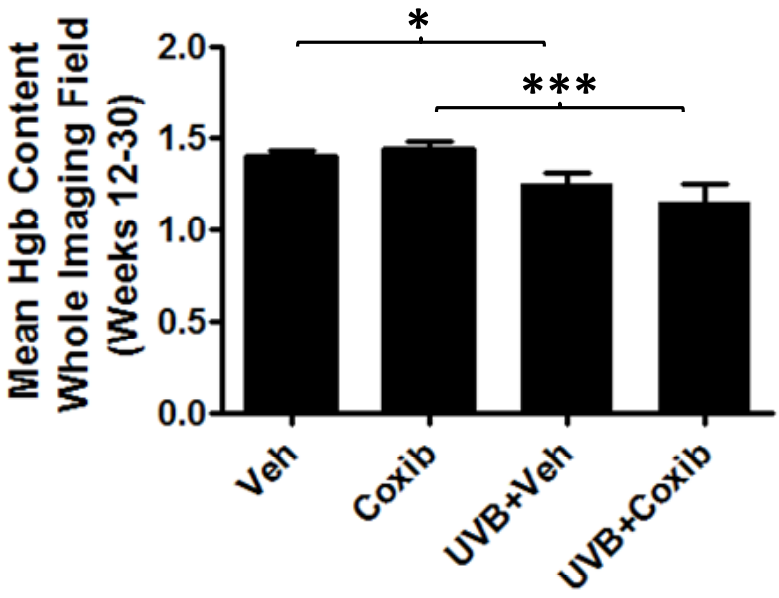


Figure S5: Overall averaged Hgb content within the imaging area fails to provide a meaningful assessment of hyperemic foci formation or the chemopreventive activity of Celecoxib. SKH-1 mice were irradiated for 10 weeks with UVB. Imaging was performed every other week after discontinuing UVB treatments and the average Hgb content in the imaging area was calculated. Results represent the time-averaged Hgb content in the imaging area from 5-8 animals per treatment group (mean and SD). UVB treated animals exhibited a statistically significant reduction in time averaged Hgb content relative to their non-irradiated treatment controls. p=0.0389 for Veh treated and p=0.0002 for Coxib treated animals, adjusted for multiple comparisons of ANOVA using Fisher's protected least significance difference.

SUPPLEMENTAL TABLE

Macroscopic Tumors in Imaging Area (% of total examined tumors)								
Experimental Group	**Papilloma Grade 1**	**Papilloma Grade 2**	**Papilloma Grade 3**	**MISCC Stage 1**	**MISCC Stage 2**	**MISCC Stage 3**	**Invasive SCC**	**Spindle Cell Carcinoma**
UVB+Acetone	46.8	17.0	6.4	6.4	6.4	8.5	6.4	2.1
UVB+Celecoxib	50	30	0	10	0	0	0	10
Microscopic Tumors / linear millimeter (Mean ± SD)								
Experimental Group	**Papilloma Grade 1**	**Papilloma Grade 2**	**Papilloma Grade 3**	**MISCC Stage 1**	**MISCC Stage 2**	**MISCC Stage 3**	**Invasive SCC**	**Spindle Cell Carcinoma**
UVB+Acetone Low Hgb	0.009 ± 0.020	0 ± 0	0 ± 0	0 ± 0	0 ± 0	0 ± 0	0 ± 0	0 ± 0
UVB+Acetone High Hgb	0.154 ± 0.104	0.031 ± 0.031	0.075 ± 0.146	0.024 ± 0.037	0 ± 0	0 ± 0	0 ± 0	0 ± 0
UVB+Celecoxib Low Hgb	0.005 ± 0.010	0 ± 0	0 ± 0	0 ± 0	0 ± 0	0 ± 0	0 ± 0	0 ± 0
UVB+Celecoxib High Hgb	0.115 ± 0.013	0.055 ± 0.064	0.013 ± 0.023	0.021 ± 0.036	0.013 ± 0.023	0 ± 0	0 ± 0	0 ± 0

Table S1: Histopathological assessment of tumor type for visible (macroscopic: top) and microscopic (subclinical or not visibly apparent) tumors seen in areas of high and low Hgb content for vehicle (acetone) or celecoxib treated mice.

SUPPLEMENTAL REFERENCES

1. Xu Z, Liu J, Hong DH, Nguyen VQ, Kim MR, Mohammed SI, et al. Back-directional gated spectroscopic imaging for diffuse light suppression in high anisotropic media and its preclinical applications for microvascular imaging. IEEE Journal of Selected Topics in Quantum Electronics. 2010;16:815 - 23.

2. Xu Z, Liu J, Kim YL. Diffuse light suppression of back-directional gating imaging in high anisotropic media. Journal of Biomedical Optics. 2009;14:030510.

3. Prahl SA, van Gemert MJC, Welch AJ. Determining the optical-properties of turbid media by using the adding-doubling method. Applied Optics. 1993;32:559-68.

4. Sahu RP, Dasilva SC, Rashid B, Martel KC, Jernigan D, Mehta SR, et al. Mice lacking epidermal PPARgamma exhibit a marked augmentation in photocarcinogenesis associated with increased UVB-induced apoptosis, inflammation and barrier dysfunction. International Journal of Cancer. 2012;131:E1055-66.

5. Benavides F, Oberyszyn TM, VanBuskirk AM, Reeve VE, Kusewitt DF. The hairless mouse in skin research. Journal of Dermatological Science. 2009;53:10-8.